Construction of spongy antimony-doped tin oxide/graphene nanocomposites using commercially available products and its excellent electrochemical performance

Xiaowei Zhao [a, b, d], Jingwei Zhang [a, b, c, *], Jiwei Zhang [a, b], Chunhong Gong [a, d], Xiufang Gu [a, b], Zhihua Ma [a, b], Jingfang Zhou [c], Laigui Yu [a, b], Zhijun Zhang [a, b, *]

[a] Key Laboratory of Ministry of Education for Special Functional Materials, Henan University, Kaifeng, 475004, PR China
[b] Collaborative Innovation Center of Nano Functional Materials and Applications, Henan Province, China
[c] Ian Wark Research Institute, University of South Australia, Mawson Lakes, SA, 5095, Australia
[d] College of Chemistry and Chemical Engineering, Henan University, Kaifeng, 475004, PR China

HIGHLIGHTS

- The spongy ATO/NG/TEPA hybrid was constructed by a one-pot hydrothermal process.
- TEPA, as a multifunctional agent, plays a crucial role.
- The commercial ATO precursor was used as raw material.
- The hybrid exhibits high electrochemical performance for lithium ion battery.

GRAPHICAL ABSTRACT

ARTICLE INFO

ABSTRACT

We construct successfully a porous antimony-doped tin oxide (ATO)/nitrogen-doped graphene 3-dimensional (3D) frameworks (denoted as ATO/NG/TEPA; TEPA refers to tetraethylenepentamine) by a one-pot hydrothermal process, with which TEPA aqueous solution is adopted to easily re-disperse commercial ATO precursor forming a transparent hydrosol. The results show that TEPA plays a key role in the construction of ATO/NG/TEPA, not only acting as a peptization reagent to re-disperse ATO precursor nanoparticles, and as a linker to combine ATO with graphene sheets. The as-fabricated ATO/NG/TEPA hybrid as the negative electrode of lithium ion batteries exhibits excellent lithium storage capacity and cycling stability. With the advantage of easily re-dispersing commercial ATO, the present synthetic route may be put into use for the large-scale production of the titled nanocomposites as the anode material of lithium ion batteries.

© 2015 Elsevier B.V. All rights reserved.

1. Introduction

Rechargeable lithium ion batteries (LIBs) are viewed as the most promising candidates for applications in portable electronics, electric vehicles (EVs) and hybrid electric vehicles [1,2] because they exhibit relatively high energy density and power density [3–5]. However, in terms of the limited capacity of commercial carbon-based anode, it is urgent to seek upgrade substitute active

* Corresponding authors. Key Laboratory of Ministry of Education for Special Functional Materials, Henan University, Kaifeng, 475004, PR China.
E-mail addresses: jwzhang@henu.edu.cn (J. Zhang), zhangzhijun@henu.edu.cn (Z. Zhang).

materials for next-generation LIBs applicable to EVs requiring higher specific capacity.

Tin-based electrode materials such as Sn, SnO_x and Sb-doped SnO_2 (ATO) have attracted numerous attention owing to their high theoretical Li storage capacity (991 mAh g^{-1} for Sn [6] and 1491 mAh g^{-1} for SnO_2 [6]). However, the practical application of tin-based material is hampered by the drastic capacity fading resulted from huge volume change [6,7] and aggregation accompanied with repeated alloying/dealloying process [8]. Fortunately, constructing graphene-based hybrid materials, especially 3-dimensional (3D) graphene/SnO_2 hybrid, is an effective strategy to buffer the volume expansion, avoid the aggregation and improve the conductivity of tin oxide, thereby promoting the electrochemical performance for LIBs [9–20].

Up to now, chlorinous tin salt such as $SnCl_2$ and $SnCl_4$ are mainly adopted as the tin sources for preparing SnO_2/graphene composites. This is because Sn^{2+} or Sn^{4+} cation originated from the aqueous solution of the tin salt can be easily adsorbed on graphene oxide (GO) sheets with the assistance of electrostatic attractive force and then transformed to crystalline SnO_2 upon hydrothermal treatment [12,19] or calcination treatment [10,14,16,17]. Unfortunately, chloride ion causes erosion of the containers especially at an elevated temperature in acid solution, which makes it imperative to adopt apparatus with excellent anticorrosion ability for preparing SnO_2/graphene composites [12,16,21,22]. In the meantime, chloride ion is difficult to be washed off from resultant products, due to its strong nucleophilicity and adsorbability [23]. Therefore, it is urgent to simplify the preparation process and reduce the production cost of SnO_2/graphene composites with $SnCl_2$ and $SnCl_4$ as the tin sources.

Considering that both SnO_2 and GO are commercially accessible products, it could be of significance to fabricate 3D SnO_2/graphene nanocomposites with commercial SnO_2 and GO as the starting materials, though this still remains a challenge. In this sense, the researches separately conducted by two research groups could be of special significance. Namely, Liang et al. and Gao et al., with commercial SnO_2 powder as the raw material, independently fabricated a free-standing SnO_2/graphene hybrid paper by simple filtration in combination with annealing in Ar flow [24] or with hydrothermal reduction in HBr acid [25]; and they reported that the as-obtained SnO_2/graphene hybrid electrodes exhibit enhanced energy storage stability. However, the irreversible agglomeration of commercial nanoparticles, always along with their drying or annealing treatment, leads to poor solution re-dispersibility and nanoscale inhomogeneity of the as-prepared SnO_2/graphene products.

To deal with the abovementioned issue associated with the fabrication of SnO_2/graphene nanocomposites, we draw attention to a facile and efficient one-pot wet-chemical process, hoping to get rid of the agglomeration of commercial SnO_2 nanoparticles thereby acquiring SnO_2/graphene nanocomposites with desired solution re-dispersibility and nanoscale homogeneity. Viewing that ATO as the electrode for LIBs possesses higher electrical conductivity and mechanical stability than SnO_2 [26,27], we choose ATO as the active anode material to construct graphene-based nanocomposites. The route to materialize this strategy, however, is challenging, because both GO sheets and ATO are highly negative charged in a wide range of pH value [28–30], and they can hardly be uniformly combined owing to electrostatic repulsion, not to mention that commercial ATO nanoparticles unavoidably tend to agglomerate. Pointing to those issues, we select tetraethylenepent amine (TEPA), a kind of polyamine, as a multifunctional agent to fabricate 3D architectural porous graphene/ATO nanocomposite as potential anode material of LIBs. Such a synthetic strategy is feasible, because, on the one hand, TEPA can act as a peptization reagent to re-disperse ATO precursor nanoparticles thereby avoiding their agglomeration. On the other hand, TEPA can also act as a linker to combine ATO with graphene oxide and as the nitrogen-doping agent of graphene thereby affording desired 3D ATO/N-doped graphene nanocomposite (ATO/NG/TEPA). This article reports the fabrication and electrochemical properties of the as-fabricated ATO/NG/TEPA nanocomposites in relation to their structural characterization by transmission electron microscopy, X-ray diffraction and X-ray photoelectron spectroscopy.

2. Experimental section

2.1. Materials

Graphite powder was purchased from Qingdao Xingyuan Colloidal Graphite Co., Ltd (Qingdao, China). Potassium permanganate ($KMnO_4$), sodium nitrate ($NaNO_3$), ethylene diamine (EDA) and TEPA were purchased from Tianjin Kermel Chemical Reagent Co., Ltd (Tianjin, China). sulfuric acid (H_2SO_4 98%), hydrogen peroxide (H_2O_2), hydrochloric acid (HCl; mass fraction: 35%) and ammonia (AM; mass fraction: 25%–28%) were bought from Luoyang Haohua Chemical Reagent Co., Ltd (Luoyang, China). The wet ATO precursor slurry (solid content: 20%; particle size: 2–3 nm) was purchased from Henan Wangwu Nanoscience and Technology Co., Ltd (Jiyuan, China), and it was prepared through a wet-chemical route in the absence of chloride reagent.

2.2. Methods

GO was prepared from natural graphite powder by modified Hummer's method [31,32]. Briefly, natural graphite powder (60 g) was mixed with $NaNO_3$ (30 g) and concentrated H_2SO_4 (1500 mL) at 0 °C, and then $KMnO_4$ (400 g) was slowly added into the mixed solution. Resultant mixed solution was stirred below 8 °C for 1 h and then heated to 45 °C and held there for 16 h. Upon completion of the reaction, 7.5 L of water and 70 mL of 30% H_2O_2 solution were sequentially added to terminate the reaction. The reaction system was washed with 5 L of dilute HCl (volume fraction: 10%) and adjusted to pH = 7 with dilute ammonia (10%), followed by dialyzing to completely remove residual Cl^- thereby affording GO sol.

The graphene/ATO hybrids were synthesized via a one-pot hydrothermal route. Typically, 2.0 g of wet ATO precursor was peptized in 30 mL of distilled water containing 1.0 mL of TEPA to form a transparent colloidal solution after a 30 min sonication. Then 20 mL of GO sol (5 mg mL^{-1}) was added into the colloidal solution under stirring for 20 min. Resultant mixture was transferred into a Teflon-lined stainless autoclave and kept at 240 °C for 24 h. At the end of the reaction, the target product, ATO/NG/TEPA nanocomposite was washed with distilled water and lyophilized. Nanocomposites ATO/NG/AM and ATO/NG/EDA were synthesized in the same manners while AM or EDA was used to replace TEPA. Similarly with ATO/NG/TEPA, ATO and NG were prepared without GO or ATO being added, respectively. Reduced graphene oxide (rGO) was obtained via the hydrothermal treatment of GO colloid. ATO/rGO was obtained in the presence of ATO precursor and GO colloid under the weak acidic condition via the same hydrothermal process as well.

2.3. Assembling battery

For assembling the working electrodes, a proper amount of active materials (as-prepared ATO/NG/TEPA, ATO/NG/AM and ATO/NG/EDA nanocomposites) was mixed with polyvinylidene difluoride (PVDF) and carbon black in N-methyl-2-pyrrolidone (NMP) solvent at a mass ratio of 80:10:10 to form homogeneous slurries. As-obtained slurries were uniformly coated onto Cu foil with a

coater, dried at 120 °C for 8 h and cut into slices as the electrodes. All the electrode slices and battery mold were dried in a vacuum oven at 60 °C for 12 h and then pressed with a double-roll compressor. Analogous batteries were assembled in an argon-filled glove box, with which a porous polypropylene film was used as the separator, a lithium sheet as the counter electrode, and 1 M $LiPF_6$ solution in the mixed solvent of ethylene carbonate (EC) and dimethyl carbonate (DMC; volume ratio of EC to DMC is 1:1) as the electrolyte.

2.4. Structural and electrochemical characterizations

The morphology of various as-prepared nanocomposites was observed with a transmission electron microscope (TEM; JSM-2010, JEOL Ltd., Japan) and scanning electron microscope (Nova NanoSEM 450, FEI company, USA). The crystallographic structure of the as-prepared products was identified by X-ray diffraction (XRD, Bruker, D8 Advanced, Germany, Cu-$K\alpha$ radiation, wavelength 0.15406 nm). The Raman spectra were recorded with a Dilor Labram-1B co-focal laser micro-Raman spectrometer (Jobin Yvon Ltd., France) at the wavelength of 632.8 nm. Nitrogen adsorption and desorption isotherms at 77.3 K were measured with a surface area and pore size analyzers (SI-MP-20, Quantachrome instruments, USA). The as-assembled batteries were galvanostatically charged and discharged at room temperature with Land CT-2001 (Wuhan, China) in a voltage range of 0.01–3.0 V *vs.* Li/Li$^+$. Thermal gravimetric analysis (TGA) was carried out on a TGA/SDTA851e system in air atmosphere (Mettler-Toledo, Switzerland).

3. Results and discussion

It is crucial that the precursors ATO and GO be well-dispersed and uniformly combined at nanoscale level in order to fabricate homogeneous graphene-based nanocomposites. Since nanoparticles unavoidably tend to aggregate during drying, we adopt ATO and GO slurries to ensure the good re-dispersibility and homogeneity of as-fabricated graphene/ATO nanocomposites. Such a strategy could be feasible, because ATO nanoparticles exhibit an isoelectric point of below pH 3.5 and are highly negative charged in a basic aqueous solution, which is helpful for ATO precipitate to be re-dispersed [33]. For example, Tour et al. found that introducing NaOH into a GO solution facilitates the generation of negative charge on GO surface [34]. Li et al. found that the introduction of moderate ammonia to the aqueous dispersion of GO gives rise to stable GO colloid, and even well-dispersed graphene colloid obtained after chemical reduction of GO can be transformed to graphene upon the addition of hydrazine [35]. In order to avoid the formation of insulating sodium stannate, in the present research we adopt ammonia and its derivatives including EDA and TEPA as the peptization reagents to prepare transparent ATO colloid.

Fig. 1 shows the dynamic light scattering (DLS) particle size distribution of ATO precursor in aqueous solutions of AM, EDA and TEPA as well as the tyndall effect of ATO precursor hydrosol in the aqueous solution of TEPA as a typical example. It can be seen that AM, EDA and TEPA are all effective peptized reagents to re-disperse ATO in aqueous solution (Fig. 1A), and the ATO colloids in AM, EDA and TEPA exhibit an average size of 3.5 nm, 4 nm and 5 nm, respectively. This indicates that the colloidal average size increases with the increase of the molecular size of the peptization reagents, which is probably because the molecules of the peptization reagents are anchored on the surface of the ATO precursor nanoparticles, and hence TEPA with the biggest molecular size among the three modifiers corresponds to the maximum colloidal average size.

Fig. 2 shows the TEM images and optical pictures of as-fabricated ATO/NG/AM (Fig. 2A), ATO/NG/EDA (Fig. 2B) and ATO/NG/TEPA (Fig. 2C) nanocomposites. It can be seen that the three kinds of as-fabricated graphene/ATO nanocomposites generally have a columnar morphology, but their morphologies are apparently different from each other (insets in Fig. 2, the original photos can be seen in supporting information, Fig. S2). Namely, the suspension of ATO/NG/AM displays characteristic blue color, which is attributed to conductive ATO. In other words, ATO/NG/AM nanocomposite is liable to phase separation at macroscopic level, since the ATO nanoparticles are not completely combined with GO and are inhomogeneously distributed on the surface of graphene sheets, as evidenced by relevant TEM image. Besides, the color of the ATO/NG/EDA suspension is slighter than that of ATO/NG/AM suspension, which indicates the amount of remanent ATO nanoparticles in the ATO/NG/EDA suspension is smaller than that in the ATO/NG/AM suspension. Differing from the abovementioned, the suspension of ATO/NG/TEPA is colorless and transparent, which indicates that the ATO nanoparticles are completely integrated with GO sheets and well-distributed on the graphene surface in this case, as evidenced by corresponding TEM image (the size of the ATO nanoparticles in ATO/NG/TEPA nanocomposite is about 10 nm). Furthermore, thermal gravimetric analysis (TGA, Fig. S1 in Supporting information) are carried out to verify how many ATO have been implanted into N-doped graphene 3D framework. The results indicated that only TEPA is capable of integrating of ATO and N-doped together. Thus, ATO/NG/TEPA has lowest weight loss ratio after being calcined in air atmosphere at 700 °C. Contrarily, ATO/NG/AM has lowest weight retention ratio, that means lots of ATO escaped from the 3D structure. These results accord with that observed on TEM and optical pictures.

In order to learn more about the reaction mechanism between ATO precursor and GO colloids, we measured the zeta potential of various colloids. As shown in Fig. 3, the basic solution (pH = 11) containing ATO precursor colloid and AM or EDA has almost the same zeta potential (−39 mV for AM and −38 mV for EDA), while the same basic solution containing GO colloid and AM or EDA has a more negative zeta potential (−47 mV for AM and −51 mV for EDA). It is well known that a zeta-potential value either more negative or positive than ±30 mV is sufficient to ensure good dispersion stability *via* charge repulsion [36]. As to the basic solutions containing AM or EDA, the zeta potential values are more negative than −30 mV, which means that the electrostatic repulsion makes it difficult for ATO and GO to be combined. Contrary to the above, the TEPA aqueous solution containing ATO colloid or GO colloid has a zeta potential values of −29 mV and −27 mV, respectively, and these zeta potential values are near to the critical value of −30 mV. As a result, ATO and GO can be well combined in the presence of TEPA.

According to colloid chemistry [36], negatively charged colloids are surrounded by counter-ions which neutralize the negative charge. The layer of counter-ions consists of two distinct parts: the inner layer, also known as the Helmholtz or Stern plane, and the diffuse layer, also known as the slipping plane. The inner monomolecular layer comprises ions and molecules strongly bonded to the nanoparticles surface *via* chemical interaction and can be considered as part of the colloids. Herein, the counter-ions in the inner layer are mainly positively charged ammonium ions formed by protonation of ammonia or amine (Eq. (1)–(3)), and the size of the ATO precursor colloids tends to increase with increasing ammonium ionic radii in the sequence of AM, EDA and TEPA, as confirmed by DLS results shown in Fig. 1A.
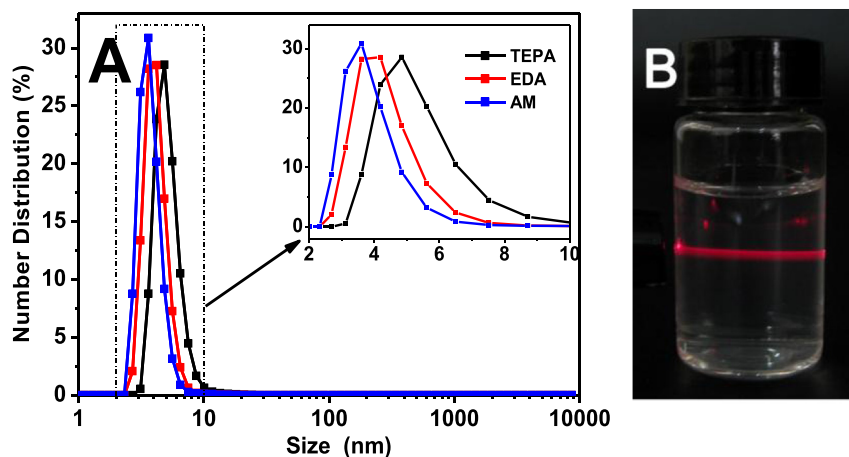
$$NH_3 + H_2O \rightarrow NH_4^+ + OH^- \qquad (1)$$

Fig. 1. DLS particle size distribution of ATO precursor in aqueous solutions of AM, EDA and TEPA (A) and tyndall effect of ATO precursor hydrosol in the aqueous solution of TEPA as a typical example (B).
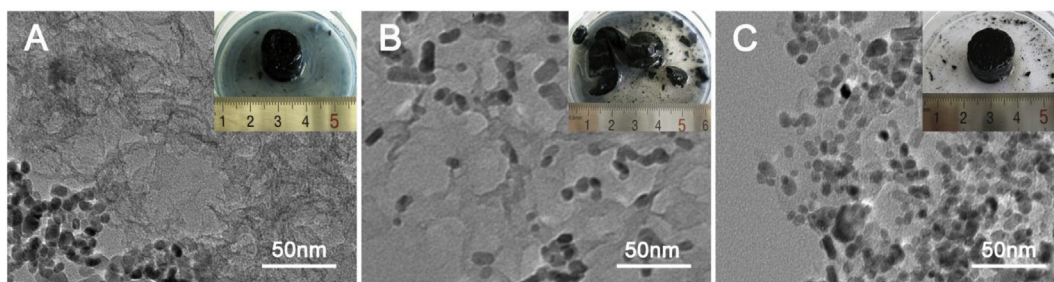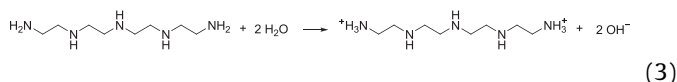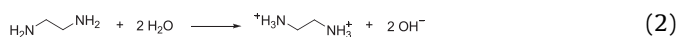

Fig. 2. TEM images and optical pictures (the insets) of as-fabricated ATO/NG/AM (A), ATO/NG/EDA (B) and ATO/NG/TEPA (C) nanocomposites.

$$H_2N{\sim}NH_2 \ + \ 2\,H_2O \ \longrightarrow \ ^+H_3N{\sim}NH_3^+ \ + \ 2\,OH^- \tag{2}$$

$$H_2N{\sim}N{\sim}N{\sim}N{\sim}NH_2 + 2\,H_2O \ \longrightarrow \ ^+H_3N{\sim}N{\sim}N{\sim}N{\sim}NH_3^+ \ + \ 2\,OH^- \tag{3}$$

A reaction mechanism is proposed as shown in Fig. 4 to explain the experimental results described above. Each ATO precursor
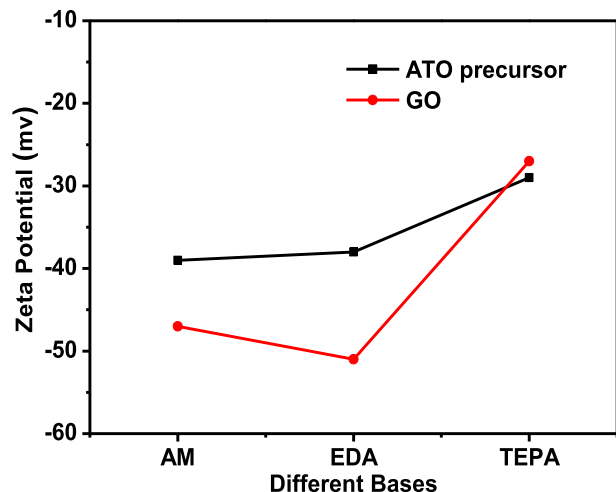

Fig. 3. Zeta potential of ATO and GO dispersed in different basic aqueous solutions (pH = 11).

colloid, being suspended in the basic aqueous solution, comprises a highly negative charged ATO core and a counter-ion shell. In the case of AM, the mutual electrostatic repulsion force between adjacent ATO precursor particles and between ATO precursor particles and GO sheets is high enough, which makes it feasible for the ATO precursor colloid to remain monodispersed in suspension even after hydrothermal treatment. When the counter ions are changed to EDA cation, the increased inner layer thickness weakens the repulsion force between the negatively charged core. More importantly, EDA molecule contains two amine groups as the "bridge", which facilitates the combination of ATO precursor nanoparticles and GO sheets. This is why fewer ATO nanoparticles remain in the suspension containing EDA than in the suspension containing AM even at the same pH value and similar zeta potential value. Furthermore, TEPA as the linker molecule exhibits a remarkably increased radius than EDA, and hence its zeta potential is reduced to approach the critical value of −30 mV. As a result, when TEPA-modified ATO precursor colloid is mixed with GO suspension, the attraction force predominates, and the ATO nanoparticles can be steadily linked with GO sheets to form an interconnected graphene-based gel during the hydrothermal reaction.

The field emission scanning electron microscopic (FE-SEM) morphology of the ATO/NG/TEPA nanocomposite and its high-resolution TEM (HRTEM) image and selected area electron diffraction (SAED) pattern are shown in Fig. 5. It can be seen that as-fabricated ATO/NG/TEPA nanocomposite contains porous 3D architectural graphene and ATO nanoparticles uniformly distributed on the graphene surface (Fig. 5A–B); and its pore size is ranged from mesopore level to macropore level. The HRTEM image clearly displays lattice fringe with an interplane spacing of 0.27 nm
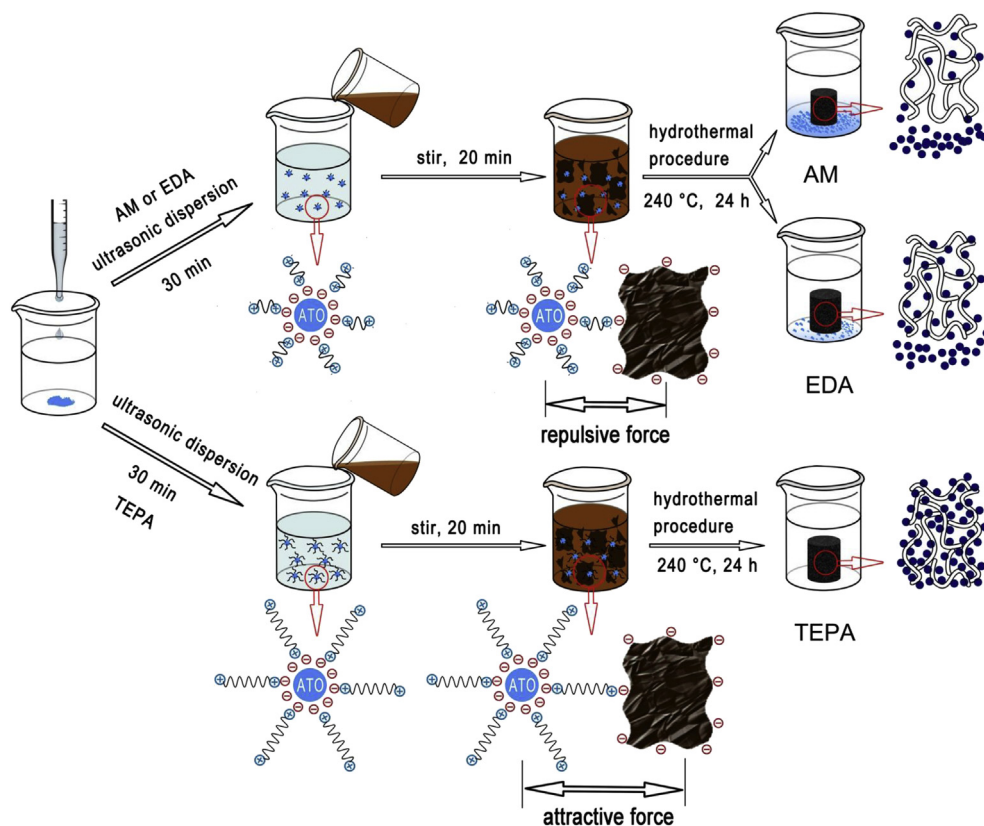
Fig. 4. Schematic diagram illustrating the possible reaction mechanism for ATO to combine with GO in the presence of AM, EDA and TEPA.

(Fig. 5C), corresponding to the (111) plane of rutile phase SnO_2; and the size of ATO nanoparticles is about 10 nm (see Figs. 2C and 5C). Corresponding SAED pattern (see the inset of Fig. 5C) proves that the ATO/NG/TEPA nanocomposite has a polycrystalline structure, and its polycrystalline rings can be ascribed to the diffraction planes of tetragonal rutile SnO_2 crystal (JCPDS No. 41-1445), which can be further confirmed by X-ray diffraction (XRD) analysis.

Recently, some researchers demonstrated that nitrogen-doping could modulate the electronic structure of graphene and introduce many vacancies and electron defects. This means N-doping may provide a feasible pathway for Li ion to penetrate into graphene layers, thereby apparently reducing the energy barrier for Li ion penetration and enhancing the lithium storage properties [15,37–39]. In the present research, we conducted XPS analyses to confirm the oxidation states of the elements in ATO/NG/TEPA nanocomposite upon nitrogen-doping. As shown in Fig. 6, the survey scan spectrum indicates that as-fabricated ATO/NG/TEPA nanocomposite contains C,O, N, Sn and Sb elements (Fig. 6A). In the meantime, the C1s core level peak can be resolved into five components centered at 284.6, 285.6, 286.5, 287.8 and 289.1 eV, respectively, and they are assigned to C=C, C–C/C=N, C–O/C–N, C=O and O–C=O, respectively (Fig. 6B) [15,37,40]. Similarly, the N1s peak can also be resolved into three components centered at 399.1, 400.1 and 401.4 eV, representing pyridinic, pyrrolic and graphitic N atoms doped in the graphene structure (Fig. 6C) [15,40,41]. These XPS data verify that the established synthetic route is feasible and efficient for synthesizing N-doped graphene. TEPA and GO will combined together *via* the attractive force as described above, subsequently, the N atoms doped into graphene sheets under high temperature and high pressure conditions during hydrothermal reaction. Besides, the $Sn3d_{5/2}$ (487.3 eV) and $Sn3d_{3/2}$ (495.7 eV) peaks [41] in Fig. 6D confirm that the Sn species in the as-fabricated nanocomposite exhibits a valence of +4. The Sb^{5+} species was confirmed by the $Sb3d_{3/2}$ peaks [42,43] (Fig. S3, supporting information).

The XRD patterns of GO, rGO, NG and ATO/NG/TEPA are shown in Fig. 7A. The diffraction peak around 10.4° (002) is the characteristic peak of GO with an interlayer spacing of 0.85 nm. This peak,
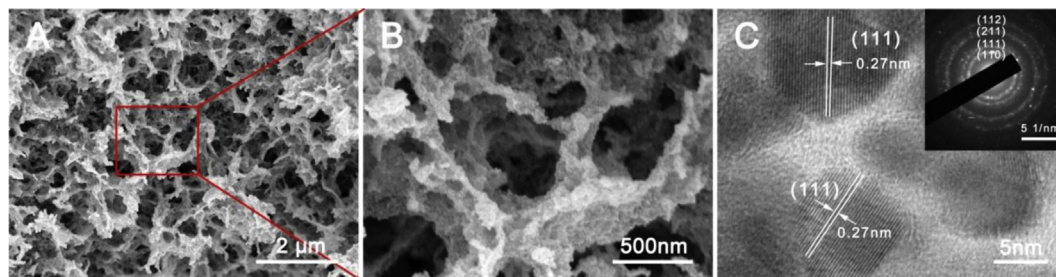

Fig. 5. FE-SEM images (A and B) and HRTEM image of the ATO/NG/TEPA nanocomposite (C). The inset is the SAED pattern of the ATO/NG/TEPA nanocomposite.
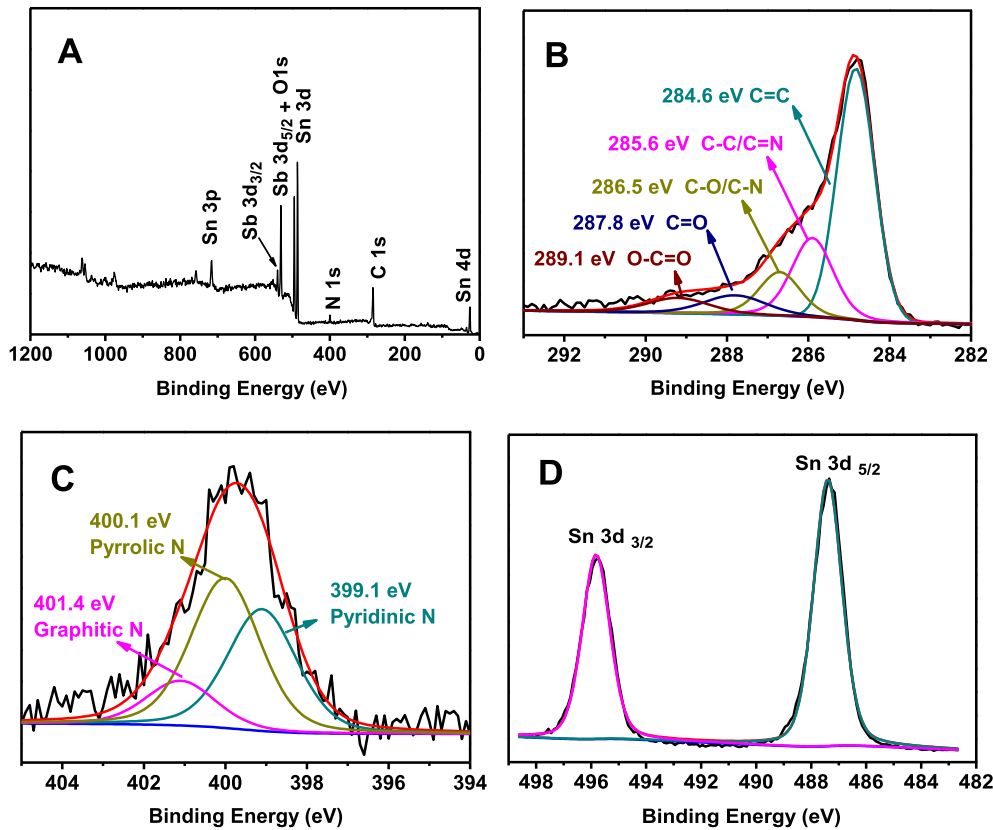
Fig. 6. XPS survey spectrum of ATO/NG/TEPA (A) and high resolution XPS spectra of C 1s (B), N 1s (C) and Sn 3d (D) of ATO/NG/TEPA.

however, is substituted by broad diffraction peaks of the graphite (002) plane in rGO and NG samples after the hydrothermal reaction, due to the deoxidization of oxygen functional groups; and corresponding broad peaks are centered at 25.6° ((002) plane with an interlayer spacing of 0.35 nm) and 23.2° ((002) plane with an interlayer spacing of 0.38 nm) [44]. This indicates that the graphene sheets in NG exhibits a larger interlayer spacing than the one in rGO, which implies that TEPA plays a key role in weakening the restack effect of graphene sheets. Besides, in combination with corresponding XPS data (Fig. 6D) and SAED pattern (inset of Fig. 5C), the diffraction patterns of ATO/NG/TEPA can be well indexed to tetragonal rutile structure of SnO_2 (JCPDS No. 41-1445). However, no obvious diffraction peaks attributed to graphene nanosheets or Sb compounds are detected for ATO/NG/TEPA nanocomposite, which means that the graphene sheets in the as-fabricated nanocomposite are well separated by ATO nanoparticles [45] and the Sb species are doped into SnO_2 crystal lattice.

Moreover, the broadened diffraction peaks indicate that there exists fine SnO_2 nanocrystal in ATO/NG/TEPA nanocomposite, and the size of SnO_2 is estimated to be about 9 nm (based on the calculation of the (110) crystalline faces of the nanocomposite with Scherrer's equation).

Raman spectroscopy is a widely used tool to distinguish ordered and disordered structure of carbonaceous materials [46]. The Raman spectra of GO, rGO, NG and ATO/NG/TEPA nanocomposite are shown in Fig. 7B. All the four samples show two characteristic peaks of graphene at 1321 cm^{-1} and 1590 cm^{-1}, corresponding to the D and G bands, respectively. The disorder induced by the amorphization of graphite has been known to cause an increase in the relative intensities of the D to G bands (I_D/I_G), as a result of a reduction in the sp^2 domain size. Obviously, the I_D/I_G value of rGO (1.28) is greater than that of GO (1.17), which implies that the average size of the sp^2 domains is reduced during hydrothermal reduction [47]. As compared with rGO, the addition of TEPA
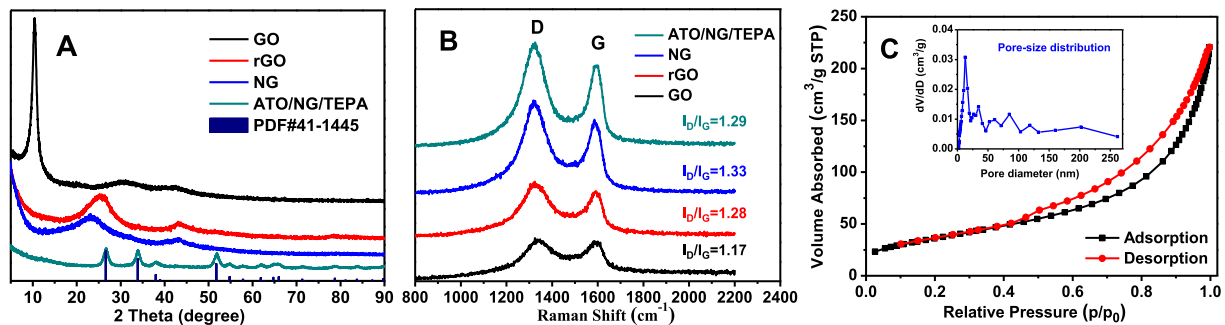

Fig. 7. XRD patterns (A) and Raman spectra (B) of GO, rGO, NG and ATO/GO/TEPA nanocomposite, N_2 adsorption/desorption isotherm curves of the nanocomposite (C).

introduces more sp^3 hybrid carbon and defects as well, thereby resulting in a higher I_D/I_G value of NG (1.33) [46,48]. As to ATO/NG/TEPA nanocomposite, the I_D/I_G ratio (1.29) is smaller than that of NG, which implies that a small amount of ATO nanoparticles are anchored on the graphene sheets, possibly through Sn−O−C bonds during the hydrothermal process. Because of the existence of Sn−O−C bonds, some of the oxygen functional groups in graphene oxide sheets is not removed, thereby resulting in larger sp^2 conjugated carbon networks like GO sheets in the as-fabricated ATO/NG/TEPA nanocomposite.

In order to investigate the porous structure and surface area of ATO/NG/TEPA hybrid, we measured the N$_2$ adsorption/desorption isotherm curves. As shown in Fig. 7C, type III adsorption and type H3 hysteresis loop are identified [49], which reveals that the ATO/NG/TEPA hybrid has porous structure attributed to 3D architectural graphene. A close observation of the inset in Fig. 7C demonstrates that the pore size of the ternary hybrid is in the range from mesopore to macropore, which is consistent with what is shown in Fig. 5A.

The electrochemical performance of the ATO/NG/TEPA nanocomposite as the anode material for LIB was investigated in a voltage window of 0.01−3.0 V vs. Li/Li$^+$. Fig. 8A shows the typical cyclic voltammogram (CV) of the ATO/NG/TEPA nanocomposite. The CV profile of the nanocomposite is substantially similar to that of SnO$_2$ [15] and ATO [50,51]. Namely, the CV curve clearly indicates a reduction peak at 0.79 V during the first discharge, which can be attributed to the formation of metallic Sn and Sb or Sn−Sb alloy in the Li$_2$O matrix [50,51]. The another strong reduction peak centrally located at about 0.1 V can be attributed to the lithiation process of Sn, Sb and C accompanying with the formation of Li$_x$Sn and Li$_y$Sb alloys $(0 \leq x \leq 4.4, 0 \leq y \leq 3)$ [15,52,53]. The oxidation peaks at 0.62 V during charging correspond to the delithiation reversible process. Similar with SnO$_2$, another oxidation peaks at 1.28 V can attribute the partially reversible reaction, which owes to small size effect of SnO$_2$ particles, SnO$_2$ + 4Li$^+$ + 4e$^-$ ↔ 2Li$_2$O + Sn [15,54], in case of bulk SnO$_2$, this reaction are commonly regarded as

irreversible process [15,55,56]. As for ATO/NG/ATO, this peak can attribute to the partially reversible reaction (Eq. (4))

$$Sn_{0.91}Sb_{0.091}O_2 + 4Li^+ + 4e^- \leftrightarrow 2Li_2O + 0.91Sn + 0.091Sb$$

$$(4)$$
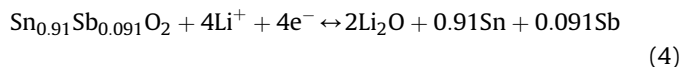
Comparing CV curve ATO/NG/TEPA with that of ATO (Fig. S4, Supporting information), it can be found that although no peaks were observed within the 2−3 V region of the CV curve, a certain capacity was still present. This capacity was attributed to the non-redox reaction process caused by the lithium storage of the large surface area and by the abundant defects in the grapheme [57].

Fig. 8B shows the representative galvanostatic charge/discharge curves of the ATO/NG/TEPA nanocomposite within increasing current densities from 100 mA g^{-1} to 5000 mA g^{-1}. The first discharge specific capacity reaches 2055 mAh g^{-1}, and a subsequent charge capacity of 1150 mAh g^{-1} with a Coulombic efficiency of 56.0% appears at a current density of 100 mA g^{-1}. The relatively low initial Coulombic efficiency for the first cycle galvanostatic charge/discharge is mainly due to the formation of a solid electrolyte interphase (SEI) film and an irreversible amorphous lithium oxide on the electrode surface [58]. Besides, the charge/discharge profiles of the ATO/NG/TEPA electrode contain plateau regions as well. Particularly, a decline voltage plateau emerges in the range of 1.3−0.5 V at the discharge step, while two plateaus appear around 0.6 V and 1.3 V in the charge curves, which are in well accordance with corresponding CV profiles (Fig. 8A).

The battery assembled with ATO/NG/TEPA nanocomposite was charged/discharged at increasing current densities from 100 mA g^{-1} to 5000 mA g^{-1} and then recycled 110 times at a constant current density of 500 mA g^{-1} to evaluate the rate capability and cycling performance. The electrochemical performance of undoped graphene/ATO (ATO/rGO) and pure ATO were evaluated as control experiments as well. As shown in Fig. 8C−D, the ATO/NG/TEPA displays superior rate capability and high cycling capability. The electrode delivers high rate specific capacities of 1233, 1104,
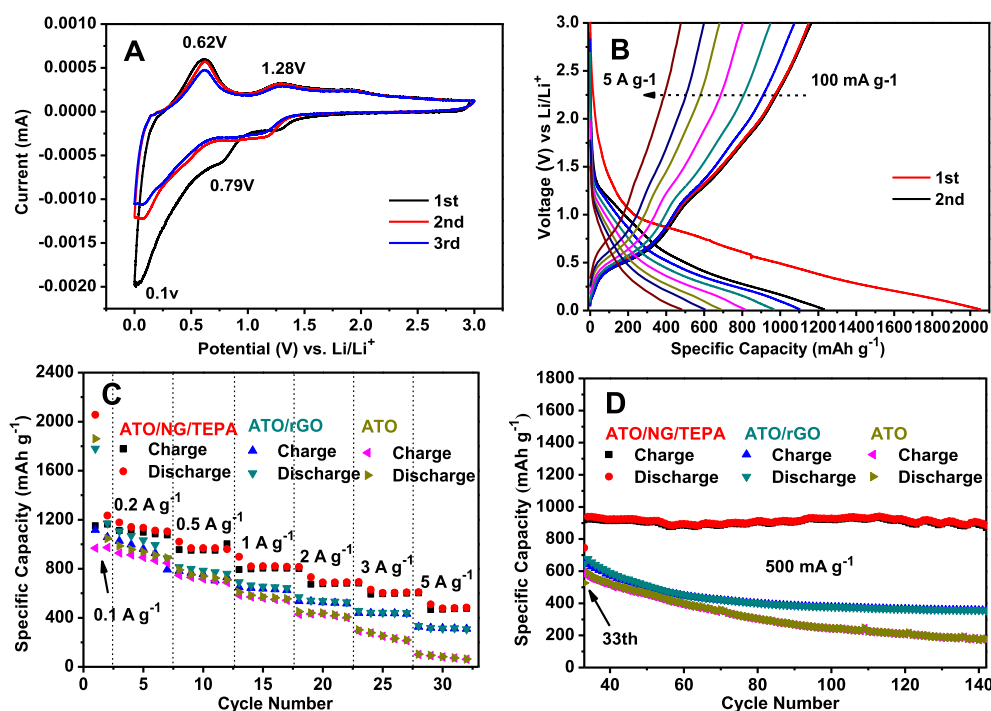

Fig. 8. Cyclic voltammogram of ATO/NG/TEPA (A), charge/discharge profiles of ATO/NG/TEPA at current densities of 100−5000 mA g^{-1} (B), rate performance at current densities of 100−5000 mAh g^{-1} (C) and the cycle performance at a current density of 0.5 A g^{-1} (D) of ATO/NG/TEPA, ATO/rGO and pure ATO.

959, 817 and 689 mAh g^{-1} at the current densities of 100, 200, 500, 1000 and 2000 mA g^{-1} after five times of cycle (twice for 100 mA g^{-1}). Even at higher current densities of 3000 mA g^{-1} and 5000 mA g^{-1}, the electrode still retains capacities of 606 mAh g^{-1} and 483 mAh g^{-1}, respectively. Furthermore, a capacity of 887 mAh g^{-1} can be recovered after another 110 times of cycles when the current density returns to 500 mA g^{-1}. This implies that the nanocomposite electrode exhibits stable structure and excellent reversibility. This performance is close to the theoretical capacity of ATO/NG/TEPA (1349 mAh g^{-1}, calculated according to Eq. (S3) in Supporting information) [15]. We suppose that the unique 3D porous architectural structure, the small size of ATO nanocrystals, and the nitrogen-doping are responsible for the enhanced rate capability and cycling performance of ATO/NG/TEPA nanocomposite. On the one hand, nitrogen doping helps to uniformly anchor ATO on graphene sheets by strong bond between nitrogen and tin dioxide, and the bond is not broken even after 20 min of ultrasonic irradiation (Fig. 2C). Therefore, ATO/NG/TEPA nanocomposite exhibits a large reversible specific capacity [15]. On the other hand, the additional defect on graphene introduced by nitrogen doping decreases the energy barrier of lithium ion and electronic penetration and transport [3,15,22], while the small size of ATO nanocrystals (~10 nm) shorten the diffusion distance of lithium ions thereby leading to a high rate specific capacity [58,59]. Moreover, the porous 3D architectural structures facilitate the penetration and diffusion of electrolyte and simultaneously accommodate the volume expansion during the lithiation process of tin [15]. These three are jointly responsible for the high electrochemical performance of the ATO/NG/TEPA nanocomposite electrode.

The ATO exhibited high reversible capacity and good rate performance because of its small size but the cycling performance is relative poor. Similarly ATO/rGO, prepared without TEPA being added, exhibited a higher rate and cycling performance than pure ATO. However, without the TEPA acting as link reagent and dopant, the graphene might just be a conductive material, thus the nanocomposite can't display most excellent electrochemical performance.

4. Conclusions

With TEPA as the "linking bridge" between GO and ATO as well as the peptizing reagent for ATO precursor and the nitrogen-doping agent for graphene, negatively charged ATO nanoparticles were successfully combined with also negatively charged GO to afford ATO/N-doped graphene nanocomposites. Thanks to the peptization of the ATO precursor in TEPA to form hydrosol, the re-disperse of commercial ATO nanoparticles is realized to provide 3D porous ATO/NG/TEPA nanocomposite containing ATO nanoparticles uniformly anchored on graphene sheets *via* one-pot hydrothermal reaction. The as-obtained ATO/NG/TEPA nanocomposite as the anode material of lithium ion batteries exhibits a high reversible charge specific capacity of 1150 mAh g^{-1} at a current density of 100 mA g^{-1} and retains a discharge specific capacity of 887 mAh g^{-1} after rate performance measurements at current densities from 100 mA g^{-1} to 5000 mA g^{-1} and subsequently additional 110 cycles of charge/discharge at a current density of 500 mAh g^{-1}. In the meantime, ATO/NG/TEPA hybrid electrode exhibits excellent power capability, delivering a discharge specific capacity of 483 mAh g^{-1} at a current density of 5000 mA g^{-1}. In terms of the commercial availability of the ATO precursor, the present synthetic route is convenient and practical for fabricating porous 3D architectural ATO-graphene nanocomposites, and it could find promising applications in large-scale production of the title nanocomposites.

Appendix A. Supplementary data

Supplementary data related to this article can be found at http://dx.doi.org/10.1016/j.jpowsour.2015.06.054.

References

[1] M. Armand, J.M. Tarascon, Nature 451 (2008) 652–657.
[2] M.S. Whittingham, Chem. Rev. 104 (2004) 4271–4302.
[3] B.P. Vinayan, S. Ramaprabhu, J. Mater. Chem. A 1 (2013) 3865–3871.
[4] J.B. Goodenough, K. Park, J. Am. Chem. Soc. 135 (2013) 1167–1176.
[5] M. Ling, J. Qiu, S. Li, H. Zhao, G. Liu, S. Zhang, J. Mater. Chem. A 1 (2013) 11543–11547.
[6] I.A. Courtney, J. Electrochem. Soc. 144 (1997) 2045–2052.
[7] T. Brousse, J. Electrochem. Soc. 145 (1998) 1–4.
[8] I.A. Courtney, J. Electrochem. Soc. 146 (1999) 59–68.
[9] X. Zhou, W. Liu, X. Yu, Y. Liu, Y. Fang, S. Klankowski, Y. Yang, J.E. Brown, J. Li, ACS Appl. Mater. Interfaces 6 (2014) 7434–7443.
[10] Z. Du, X. Yin, M. Zhang, Q. Hao, Y. Wang, T. Wang, Mater. Lett. 64 (2010) 2076–2079.
[11] H. Kim, S. Park, S. Yoon, C. Lee, J.H. Jeong, K.C. Roh, K. Kim, Chem. Mater. 26 (2014) 4838–4843.
[12] Y. Huang, D. Wu, S. Han, S. Li, L. Xiao, F. Zhang, X. Feng, ChemSusChem 6 (2013) 1510–1515.
[13] Y. Huang, D. Wu, J. Wang, S. Han, L. Lv, F. Zhang, X. Feng, Small 10 (2014) 2226–2232.
[14] S. Paek, E. Yoo, I. Honma, Nano Lett. 9 (2009) 72–75.
[15] R. Wang, C. Xu, J. Sun, L. Gao, H. Yao, ACS Appl. Mater. Interfaces 6 (2014) 3427–3436.
[16] J. Liang, Y. Liu, L. Guo, L. Li, RSC Adv. 3 (2013) 11489–11492.
[17] B. Zhang, Q.B. Zheng, Z.D. Huang, S.W. Oh, J.K. Kim, Carbon 49 (2011) 4524–4534.
[18] P. Lian, J. Wang, D. Cai, L. Ding, Q. Jia, H. Wang, Electrochim. Acta 116 (2014) 103–110.
[19] R. Liang, H. Cao, D. Qian, J. Zhang, M. Qu, J. Mater. Chem. 21 (2011) 17654–17657.
[20] K. Shiva, H.B. Rajendra, K.S. Subrahmanyam, A.J. Bhattacharyya, C.N.R. Rao, Chem. Eur. J. 18 (2012) 4489–4494.
[21] S.J.R. Prabakar, Y. Hwang, E. Bae, S. Shim, D. Kim, M.S. Lah, K. Sohn, M. Pyo, Adv. Mater. 25 (2013) 3307–3312.
[22] C. Xu, J. Sun, L. Gao, Nanoscale 4 (2012) 5425–5430.
[23] M.A. Pletnev, S.G. Morozov, V.P. Alekseev, Prot. Met. 36 (2000) 202–208.
[24] J. Liang, Y. Zhao, L. Guo, L. Li, ACS Appl. Mater. Interfaces 4 (2012) 5742–5748.
[25] T. Gao, K. Huang, X. Qi, H. Li, L. Yang, J. Zhong, Ceram. Int. 40 (2014) 6891–6897.
[26] J. Santos-Pena, T. Brousse, L. Sanchez, J. Morales, D.M. Schleich, J. Power Sources 97–98 (2001) 232–234.
[27] P. Ouyang, H. Zhang, Y. Wang, W. Chen, Z. Li, Electrochim. Acta 130 (2014) 232–238.
[28] J.S. Park, S.M. Cho, W. Kim, J. Park, P.J. Yoo, ACS Appl. Mater. Interfaces 3 (2011) 360–368.
[29] X. Huang, B. Sun, D. Su, D. Zhao, G. Wang, J. Mater. Chem. A 2 (2014) 7973–7979.
[30] S.A. Hasan, E.K. Tsekoura, V. Sternhagen, M. Strømme, J. Phys. Chem. C 116 (2012) 6530–6536.
[31] W.S. Hummers, R.E. Offeman, J. Am. Chem. Soc. 80 (1958), 1339–1339.
[32] T. Zhou, F. Chen, K. Liu, H. Deng, Q. Zhang, J. Feng, Q. Fu, Nanotechnology 22 (2011) 1–6.
[33] H. Dang, X.W. Zhao, C. Qun, J.W. Zhang, C. Chang, K.Q. Li, X.Y. Wei, Z.S. Wu, J. Funct. Mater. (2012) 3058–3062.
[34] A.M. Dimiev, L.B. Alemany, J.M. Tour, ACS Nano 7 (2013) 576–588.
[35] D. Li, M.B. Müller, S. Gilje, R.B. Kaner, G.G. Wallace, Nat. Nanotechnol. 3 (2008) 101–105.
[36] D.H. Everett, The Royal Society of Chemistry, London, 1988.
[37] X. Zhou, L. Wan, Y. Guo, Adv. Mater. Weinh. Ger. 25 (2013) 2152–2157.
[38] Y. Yu, Phys. Chem. Chem. Phys. 15 (2013) 16819–16827.
[39] Y.F. Li, Z. Zhou, L.B. Wang, J. Chem. Phys. 129 (2008) 104703–104705.

[40] J. Liang, Z. Cai, Y. Tian, L. Li, J. Geng, L. Guo, ACS Appl. Mater. Interfaces 5 (2013) 12148—12155.
[41] X. Wang, X. Cao, L. Bourgeois, H. Guan, S. Chen, Y. Zhong, D. Tang, H. Li, T. Zhai, L. Li, Y. Bando, D. Golberg, Adv. Funct. Mater. 22 (2012) 2682—2690.
[42] W.E. Morgan, W.J. Stec, J.R. Van Wazer, Inorg. Chem. 12 (1973) 953—955.
[43] F. Garbassi, Surf. Interface Anal. 2 (1980) 165—169.
[44] H. Guo, P. Su, X. Kang, S. Ning, J. Mater. Chem. A 1 (2013) 2248—2255.
[45] H. Liu, J. Huang, C. Xiang, J. Liu, X. Li, J. Mater. Sci. Mater. Electron 24 (2013) 3640—3645.
[46] A. Eckmann, A. Felten, I. Verzhbitskiy, R. Davey, C. Casiraghi, Phys. Rev. B 88 (2013) 035426/1—035426/11.
[47] B. Lee, S.C. Han, M. Oh, M.S. Lah, K. Sohn, M. Pyo, Electrochim. Acta (2013) 149—155.
[48] K.N. Kudin, B. Ozbas, H.C. Schniepp, R.K. Prud'Homme, I.A. Aksay, R. Car, Nano Lett. 8 (2008) 36—41.
[49] K.S.W. Sing, Pure Appl. Chem. 57 (1985) 603—619.
[50] Y. Wang, T. Chen, Electrochim. Acta 54 (2009) 3510—3515.
[51] Y. Wang, I. Djerdj, B. Smarsly, M. Antonietti, Chem. Mater. 21 (2009) 3202—3209.
[52] S. Park, S. Seo, S. Lee, S.W. Seo, K. Park, C.W. Lee, D. Kim, K.S. Hong, J. Phys. Chem. C 116 (2012) 21717—21726.
[53] O. Cevher, U. Tocoglu, H. Akbulut, Int. J. Hydrogen Energy 39 (2014) 21429—21434.
[54] Q. Guo, Z. Zheng, H. Gao, J. Ma, X. Qin, J. Power Sources 240 (2013) 149—154.
[55] P. Lian, X. Zhu, S. Liang, Z. Li, W. Yang, H. Wang, Electrochim. Acta 56 (2011) 4532—4539.
[56] J. Tang, J. Yang, L. Zhou, J. Xie, G. Chen, X. Zhou, J. Mater. Chem. A 2 (2014) 6292—6295.
[57] N. Li, H. Sonsg, H. Cui, C. Wang, Electrochim. Acta 130 (2014) 670—678.
[58] F. Ye, B. Zhao, R. Ran, Z. Shao, Chem. Eur. J. 20 (2014) 4055—4063.
[59] Y. Chen, B. Song, R.M. Chen, L. Lu, J. Xue, J. Mater. Chem. A 2 (2014) 5688—5695.